Journal of Dynamics, Monitoring and Diagnostics, 2024, 3, 143-155
https://doi.org/10.37965/jdmd.2024.527

ISTP
RESEARCH ARTICLE

Time-Varying Mesh Stiffness Calculation and Dynamic Modeling of Spiral Bevel Gear with Spalling Defects

Keyuan Li,[1,2] Baijie Qiao,[1,2] Heng Fang,[1,2] Xiuyue Yang,[1,2] and Xuefeng Chen[1,2]
[1]School of Mechanical Engineering, Xi'an Jiaotong University, Xi'an, PR China
[2]National Key Lab of Aerospace Power System and Plasma Technology, Xi'an Jiaotong University, Xi'an, PR China

(Received 01 April 2024; Revised 13 May 2024; Accepted 06 June 2024; Published online 06 June 2024)

Abstract: Time-varying mesh stiffness (TVMS) is a vital internal excitation source for the spiral bevel gear (SBG) transmission system. Spalling defect often causes decrease in gear mesh stiffness and changes the dynamic characteristics of the gear system, which further increases noise and vibration. This paper aims to calculate the TVMS and establish dynamic model of SBG with spalling defect. In this study, a novel analytical model based on slice method is proposed to calculate the TVMS of SBG considering spalling defect. Subsequently, the influence of spalling defect on the TVMS is studied through a numerical simulation, and the proposed analytical model is verified by a finite element model. Besides, an 8-degrees-of-freedom dynamic model is established for SBG transmission system. Incorporating the spalling defect into TVMS, the dynamic responses of spalled SBG are analyzed. The numerical results indicate that spalling defect would cause periodic impact in time domain. Finally, an experiment is designed to verify the proposed dynamic model. The experimental results show that the spalling defect makes the response characterized by periodic impact with the rotating frequency of spalled pinion.

Keywords: dynamic modeling; slice method; spalling; spiral bevel gear; time-varying mesh stiffness (TVMS)

I. INTRODUCTION

The spiral bevel gear (SBG) has substantial advantages over spur gear and helical gear, including high contact ratio, high load bearing capacity, smooth transmission, compact structure, and lower noise [1]. Because of these merits, the SBG has been widely applied in the situations where transmission space is limited, and motion or power needs to be transmitted between intersecting shafts, particularly in the transmission systems of helicopters [2]. However, owing to heavy service loads, deterioration of lubrication, and other bad operating conditions, spalling fault may develop on the tooth surface [3–6], which may alter the time-varying mesh stiffness (TVMS) and effect the dynamic performance in SBG transmission system [7–9]. Gear spalling fault can also be the important cause of serious damage to the gear transmission systems [10]. TVMS is one of the inevitable internal excitations of the SBG transmission system. And it is also a key parameter for both the structural strength calculation of SBG and its dynamic analysis [11–13]. Currently, the spalling mechanism of SBG has not been explained clearly. Besides, due to the spatial curved surface and the complex geometric relationship of SBG, how to evaluate the TVMS of SBG with spalling defect becomes an urgent problem.

In the past decades, many scholars have carried out studies to investigate the TVMS of gears with spalling defect. Among them, finite element method (FEM) and analytical method (AM) are the two main methods employed to gain the mesh stiffness of spalled gear pair. Compared to FEM, AM is easier to implement and has higher computing efficiency with acceptable accuracy. In early studies, the spalling defects are mostly modeled as simple regular shapes, such as circles and rectangles. Charri *et al.* [14] and Ma *et al.* [15] evaluated the mesh stiffness of spalling fault with rectangle shape for spur gears. Jiang *et al.* [16] presented a rectangular-shaped spalling model to calculate the mesh stiffness of helical gear under spalling condition, and the influences of spalling size on dynamic characteristics were investigated in their work. Saxena *et al.* [17] proposed an AM for the calculation of the TVMS of spur gears with various spalling shapes. Liang *et al.* [9] simulated tooth pits as circle shape, and three pitting damage levels were defined by different number of pits. However, the regular spall shape is usually quite different from the actual engineering conditions. In [4,7], a new pitting model with multiple pits was adopted using a probability distribution, to study the effects of different pitting severity levels on TVMS. Luo *et al.* [18] developed a shape-independent spalling model to calculate the TVMS of spur gear pair with an irregular spalling. In this study, two defect ratios were used to model the characteristics and severity levels of the spalling defect. Wu *et al.* [19] evaluated the mesh stiffness of helical gears with spalling faults that had curved-bottom features. The spalling defect was modeled in ellipsoid geometrical shape, and the correctness and effectiveness of the model were validated through FEM.

The aforementioned researches are mainly based on spur gears or helical gears. For SBG, its complex tooth flank flexural behaviors make it show excellent load-carrying abilities [20]. However, the complex mesh relationship and spatial curved surface also make it difficult to evaluate the TVMS directly utilizing the potential energy method [21]. Meanwhile, the study on the calculation method of TVMS with spalling defects is still limited. In recent years, some researchers have presented a new AM called the slice method for TVMS calculation. The core idea of the slice

Corresponding author: Baijie Qiao (e-mail: qiao1224@xjtu.edu.cn).

method is partitioning the gear tooth into a series of spur gears whose width is very thin along the tooth width direction, and then the TVMS of gears can be obtained through summing the TVMS of the spur gear slices [22]. Chen *et al.* [23] proposed a mesh stiffness calculation model by dividing the gear tooth into independent thin pieces to study the effects crack faults on gear mesh stiffness. Wan *et al.* [24] used slice method to calculate mesh stiffness of helical gears. Feng *et al.* [25] assessed slice method to evaluate the TVMS of helical gear pairs, where the effects of gear tooth width, gear helix angle, friction coefficient, and gear modification coefficient were analyzed. With slice method, Yu and Mechefske [26] proposed an improved model to evaluate the single mesh stiffness of helical gears with the consideration of coupling effect between neighboring tooth slices. Wang and Zhang [27] developed a helical gear TVMS model considering tooth profile errors through slice method, and they discussed the influences of profile modifications on stress and mesh stiffness. Sun *et al.* [28] proposed a computational method to calculate the mesh stiffness of straight beveloid gear with a pitting defect with the use of slice principle and effectiveness of the method was verified through FEM. Liu *et al.* [29] used loaded tooth contact analysis to analyze the meshing of SBGs, in which the tooth was sliced. Mo *et al.* [30] calculated the tooth deformation of asymmetric gear slice and provided an improved AM for the TVMS model. It can be seen from the above literature survey that the slice method has been successfully applied to calculate mesh stiffness of spur gears, helical gears, and spur bevel gears, and it exhibits significant potential in calculation of TVMS for SBG. Nevertheless, the slice method has not been utilized in the calculation of TVMS for the SBG with spalling defect.

In the fields of SBG dynamic modeling, Yavuz *et al.* [31] studied the nonlinear problem in SBG system and proposed a time-varying dynamical model, which considered the influences from shafts and bearings stiffness. Yang *et al.* [32] developed a new methodology for gear surface modification to enhance the transmission performance of hypoid gears and SBG. An 8-degrees-of-freedom (DOF) nonlinear dynamic model was established by Li *et al.* [33] to investigate the effects of asymmetric mesh stiffness on SBG system, and the model also included factors of TVMS, tooth backlash, and transmission error. Tang *et al.* [3] proposed a nonlinear dynamic model of bevel gear system combining TVMS and backlash and investigated the influences of static transmission error on the response characteristics of bevel gears. Cao *et al.* [34] proposed a tribo-dynamic model for SBG system. The model combined a mixed lubrication model with an 8-DOF nonlinear model using an iterative numerical method. Chen *et al.* [35] proposed an analytical model to obtain the nonlinear excitation and loaded mesh characteristics of SBGs. Molaie *et al.* [36] investigated the nonlinear dynamics of the SBG with backlash. The FEM was employed to get the accurate mesh stiffness, and the nonlinear dynamic behavior was analyzed through the nonlinear and time-dependent parametrically excited dynamic model. The aforementioned work mainly focuses on the dynamics of the SBG in perfect condition. However, the dynamic modeling of the SBG with spalling defects remains a critical issue that has not been fully studied.

This study focuses on the calculation of the TVMS of the SBG afflicted by spalling defects and studies the influence of the spalling defect on the vibration responses of the SBG transmission system. The main contributions of this paper can be summarized as:

- The slice method is employed to model the spalling fault of the spiral bevel gear pair (SBGP).
- The potential energy method is adopted to derive the calculation formula of TVMS for the SBG with spalling defects. The effects of the spalling defects on TVMS are studied.
- A dynamic model with 8 DOF for SBG is established by incorporating TVMS with spalling defects to reveal the influences of tooth spalling on vibration responses of SBG system.

The sections of this paper are organized as follows: Section II calculates the TVMS for spalled SBG with slice method. In Section III, the TVMS of spalled gears in several cases is evaluated to illustrate the model proposed in Section II. The results are validated by FEM. Section IV establishes a dynamic model for the SBG system with spalling defects, and experimental verification is carried out. Several conclusions are drawn in Section V.

II. TVMS CALCULATION OF SBG WITH SPALLING DEFECT

A. MODEL FORMULATION OF SPALLING

In this study, the SBGP is divided into N independent slices with equal distances along the tooth width. Here, w and $\Delta w = w/N$ represent the width of tooth and slice, respectively. It is assumed that the slices are sequentially numbered from the outer face to the inner face of the gear. Defining the slice on outer face as the first slice, and the slice on inner face as the last, the gear slice model is shown in Fig. 1. When the number of slices is substantial enough, each slice could be approximated as a thin straight bevel gear. This approximation allows it to be treated as an equivalent spur gear. Then the mesh stiffness of each slice gear pair can be evaluated with the potential energy method, and the mesh stiffness of SBG can be obtained by summing the stiffness of the slice gear pairs in mesh.

Due to harsh working conditions and insufficient lubrication, tooth spalling will occur on gear tooth surface. Generally speaking, spalling fault has an irregular shape in industrial practice. However, to simplify the establishment of the fault model, the spalling is assumed to be a

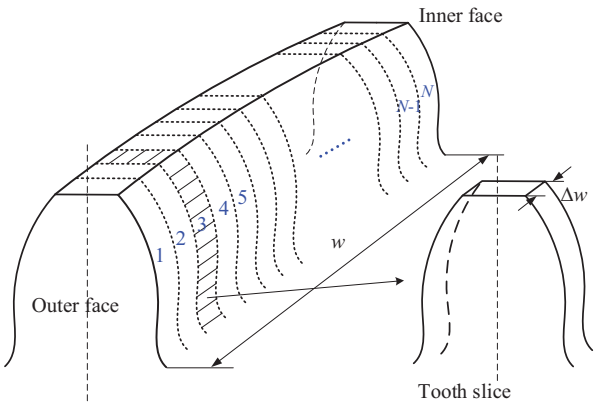

Fig. 1. Schematic diagram of tooth slice.

rectangle shape in this study as presented in Fig. 2. Meanwhile, considering the fact that most spalling defects occur nearby the pitch line of the driving gear (pinion), it is assumed that the spalling occurs on the driving gear, centered on the tooth pitch line, and distributed along the tooth width. The size of the spalling fault can be completely defined by three variables: spalling depth h_s, spalling length l_s, and spalling width w_s.

The angle range of the spalling region of the tooth slice can be determined through Fig. 3. Using the slice method to divide the tooth into N slices, the cantilever beam model for the slice with spalling is displayed in Fig. 3. For the spalled slice, the spalling width w_{ks} and depth h_{ks} are equal to w_s and h_s, and the length is Δw. The spalling region AC is centered on the pitch line, which can be defined by angles α_{ka} and α_{kc}.The two angles can be obtained by following equations:

$$\alpha_{kp} = \tan\alpha_{tk} - \alpha_{k2} \tag{1}$$

$$L_{A1} = L_{A2} - w_{ks} \tag{2}$$

$$L_{C1} = L_{C2} + w_{ks} \tag{3}$$

$$L_{A1} = 2r_{kb}((\alpha_{k2} + \alpha_{ka})\sin\alpha_{ka} + \cos\alpha_{ka}) \tag{4}$$

$$L_{A2} = 2r_{kb}((\alpha_{k2} + \alpha_{kp}) + \cos\alpha_{kp}) \tag{5}$$

$$L_{C1} = 2r_{kb}((\alpha_{k2} + \alpha_{kc})\sin\alpha_{kc} + \cos\alpha_{kc}) \tag{6}$$

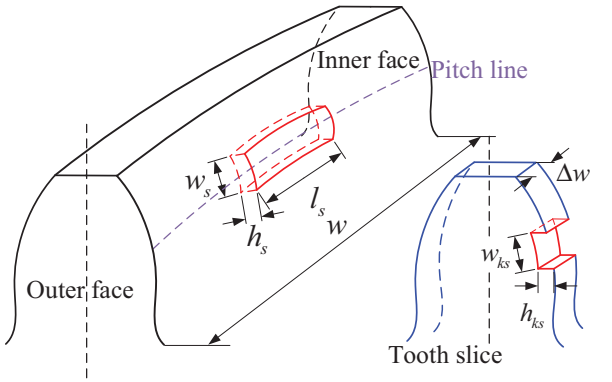

Fig. 2. Model of the spalled tooth.

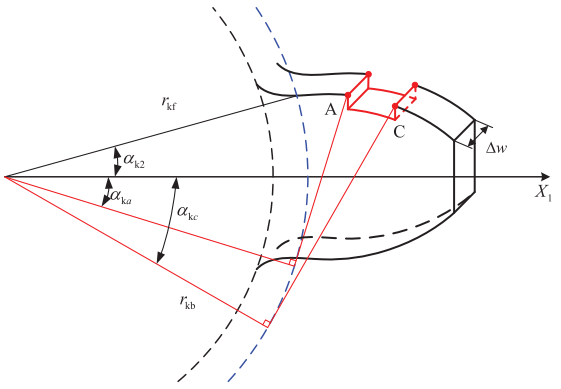

Fig. 3. Cantilever beam model of spalled slice.

$$L_{C2} = 2r_{kb}((\alpha_{k2} + \alpha_{kp}) + \cos\alpha_{kp}) \tag{7}$$

where α_{kp} represents the pitch circle angle of the k^{th} slice gear and α_{k2} represents the half tooth angle of the base circle.

B. TVMS CALCULATION OF SPALLED SBG

1) MESH STIFFNESS OF SPALLED GEAR SLICE. The pinion of the SBGP has fewer teeth compared with the driven gear, which means that the teeth of pinion will engage more frequently. It is more likely to suffer from spalling defect on the pinion. Therefore, in this study, it is assumed that the spalling defect only appears on the tooth face of the pinion. Meanwhile, for external spur gear, the base circle usually does not coincide with the root circle. According to the basic gear geometry, if the number of teeth is less than 41, the base circle is larger, or the root circle is larger. The two cases will be analyzed separately in this section. For each case, according to the different meshing states, three situations will be discussed, respectively.

Case 1: The root circle is smaller than the base circle
Situation A: $\alpha_{k1} \geq \alpha_{kc}$
Figure 4 shows the cantilever beam model of spalled tooth model when the root circle is smaller than the base circle. The expressions of the area A_{kx} and the area moment of inertia of the section I_{kx} in the involute part and the area A_{dk1} and the area moment of inertia of the section I_{dk1} in the transition curve part can be written as follows:

$$A_{ks} = (2h_{kx})\Delta w \tag{8}$$

$$I_{kx} = (2h_{kx})^3\Delta w/12 \tag{9}$$

$$A_{dk1} = (2r_{kb}\sin\alpha_{k2})\Delta w \tag{10}$$

$$I_{kx} = (2r_{kb}\sin\alpha_{k2})^3\Delta w/12 \tag{11}$$

where the specific meaning and expressions of h_k, h_{kx}, and α_{k2} can be found in [37].
The area A_{kxs} and the area moment of inertia I_{kxs} and at the section of x_k in spalling region can be written as:

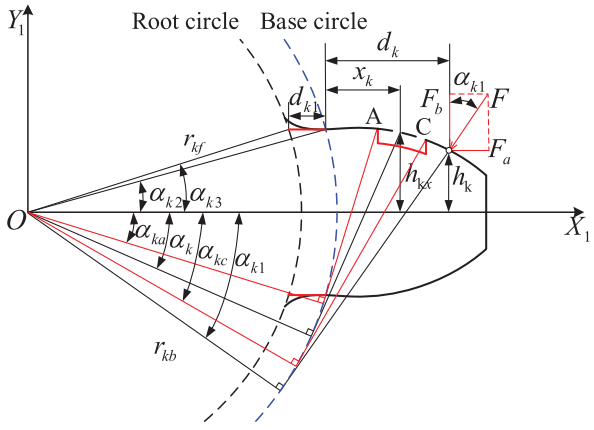

Fig. 4. Spalled sliced gear model when the root circle is smaller than base circle.

$$A_{kxs} = (2h_{kx} - h_{ks})\Delta w \tag{12}$$

$$I_{kxs} = (2h_{kx} - h_{ks})^3 \Delta w/12 \tag{13}$$

With the use of the potential energy method [7,38], the bending stiffness k_{kb}, shear stiffness k_{ks}, and axial compressive stiffness k_{ka} can be expressed as follows:

$$\begin{aligned}\frac{1}{k_{kb}} = &\int_{-\alpha_{k1}}^{-\alpha_{kc}} \frac{[(d_k - x_k)\cos\alpha_{k1} - H_k]^2 r_{kb}\theta_k}{EI_{kx}} \mathrm{d}\alpha_k \\ &+ \int_{-\alpha_{kc}}^{-\alpha_{ka}} \frac{[(d_k - x_k)\cos\alpha_{k1} - H_k]^2 r_{kb}\theta_k}{EI_{kxs}} \mathrm{d}\alpha_k \\ &+ \int_{-\alpha_{ka}}^{\alpha_{k2}} \frac{[(d_k - x_k)\cos\alpha_{k1} - H_k]^2 r_{kb}\theta_k}{EI_{kx}} \mathrm{d}\alpha_k \\ &+ \int_{0}^{d_{k1}} \frac{[(d_k + x_k)\cos\alpha_{k1} - H_k]^2}{EI_{dk1}} \mathrm{d}x_k\end{aligned} \tag{14}$$

$$\begin{aligned}\frac{1}{k_{ks}} = &\int_{-\alpha_{k1}}^{-\alpha_{kc}} \frac{1.2\cos^2\alpha_{k1} r_{kb}\theta_k}{GA_{kx}} \mathrm{d}\alpha_k \\ &+ \int_{-\alpha_{kc}}^{-\alpha_{ka}} \frac{1.2\cos^2\alpha_{k1} r_{kb}\theta_k}{GA_{kxs}} \mathrm{d}\alpha_k \\ &+ \int_{-\alpha_{ka}}^{\alpha_{k2}} \frac{1.2\cos^2\alpha_{k1} r_{kb}\theta_k}{GA_{kx}} \mathrm{d}\alpha_k + \frac{1.2\cos^2\alpha_{k1} d_{k1}}{GA_{dk1}}\end{aligned} \tag{15}$$

$$\begin{aligned}\frac{1}{k_{ka}} = &\int_{-\alpha_{k1}}^{-\alpha_{kc}} \frac{\sin^2\alpha_{k1} r_{kb}\theta_k}{EA_{kx}} \mathrm{d}\alpha_k + \int_{-\alpha_{kc}}^{-\alpha_{ka}} \frac{\sin^2\alpha_{k1} r_{kb}\theta_k}{EA_{kxs}} \mathrm{d}\alpha_k \\ &+ \int_{-\alpha_{ka}}^{\alpha_{k2}} \frac{\sin^2\alpha_{k1} r_{kb}\theta_k}{EA_{kx}} \mathrm{d}\alpha_k + \frac{\sin^2\alpha_{k1} d_{k1}}{EA_{dk1}}\end{aligned} \tag{16}$$

$$H_k = h_k \sin\alpha_{k1} \tag{17}$$

$$\theta_k = (\alpha_{k2} - \alpha_k)\cos\alpha_k \tag{18}$$

where the angles α_{ka} and α_{kc} can be obtained from equations Eq. (2) to Eq. (7). The meaning of a_{k1}, x_k, d_k, and d_{k1} can be seen in [37]. E and G represent Young's modulus and shear modulus, respectively.

According to the derivation in [39], the Hertzian contact stiffness is

$$k_{kh} = E^{0.9}\Delta w^{0.8} F_k^{0.1}/1.275 \tag{19}$$

where F_k represents meshing force.

The equation of fillet foundation stiffness is expressed as follows:

$$\begin{aligned}\frac{1}{k_{kf}} = &\frac{\cos^2\alpha_{tk}}{E\Delta w}\{L^*(u_{kf}/S_{kf})^2 \\ &+ M^*(u_{kf}/S_{kf}) + P^*(1 + Q^*\tan^2\alpha_{tk})\}\end{aligned} \tag{20}$$

where parameters u_{kf}, S_{kf}, L^*, M^*, P^*, and Q^* can be found in [40].

Situation B: $\alpha_{ka} < \alpha_{k1} < \alpha_{kc}$

In this situation, there is no contact between the teeth. Therefore, the Hertzian stiffness is 0. The expressions of the k_{kb}, k_{ks} and k_{ka} have changed as:

$$\begin{aligned}\frac{1}{k_{kb}} = &\int_{-\alpha_{k1}}^{-\alpha_{ka}} \frac{[(d_k - x_k)\cos\alpha_{k1} - H_k]^2 r_{kb}\theta_k}{EI_{kxs}} \mathrm{d}\alpha_k \\ &+ \int_{-\alpha_{ka}}^{\alpha_{k2}} \frac{[(d_k - x_k)\cos\alpha_{k1} - H_k]^2 r_{kb}\theta_k}{EI_{kx}} \mathrm{d}\alpha_k \\ &+ \int_{0}^{d_{k1}} \frac{[(d_k + x_k)\cos\alpha_{k1} - H_k]^2}{EI_{dk1}} \mathrm{d}x_k\end{aligned} \tag{21}$$

$$\begin{aligned}\frac{1}{k_{ks}} = &\int_{-\alpha_{k1}}^{-\alpha_{ka}} \frac{1.2\cos^2\alpha_{k1} r_{kb}\theta_k}{GA_{kxs}} \mathrm{d}\alpha_k \\ &+ \int_{-\alpha_{ka}}^{\alpha_{k2}} \frac{1.2\cos^2\alpha_{k1} r_{kb}\theta_k}{GA_{kx}} \mathrm{d}\alpha_k + \frac{1.2\cos^2\alpha_{k1} d_{k1}}{GA_{dk1}}\end{aligned} \tag{22}$$

$$\begin{aligned}\frac{1}{k_{ka}} = &\int_{-\alpha_{k1}}^{-\alpha_{ka}} \frac{\sin^2\alpha_{k1} r_{kb}\theta_k}{EA_{kxs}} \mathrm{d}\alpha_k \\ &+ \int_{-\alpha_{ka}}^{\alpha_{k2}} \frac{\sin^2\alpha_{k1} r_{kb}\theta_k}{EA_{kx}} \mathrm{d}\alpha_k + \frac{\sin^2\alpha_{k1} d_{k1}}{EA_{dk1}}\end{aligned} \tag{23}$$

Situation C: $\alpha_{k1} \le \alpha_{ka}$

In this situation, the formulas of k_b, k_s, and k_a are as follows:

$$\begin{aligned}\frac{1}{k_{kb}} = &\int_{-\alpha_{k1}}^{\alpha_{k2}} \frac{[(d_k - x_k)\cos\alpha_{k1} - H_k]^2 r_{kb}\theta_k}{EI_{kx}} \mathrm{d}\alpha_k \\ &+ \int_{0}^{d_{k1}} \frac{[(d_k + x_k)\cos\alpha_{k1} - H_k]^2}{EI_{dk1}} \mathrm{d}x_k\end{aligned} \tag{24}$$

$$\frac{1}{k_{ks}} = \int_{-\alpha_{k1}}^{\alpha_{k2}} \frac{1.2\cos^2\alpha_{k1} r_{kb}\theta_k}{GA_{kx}} \mathrm{d}\alpha_k + \frac{1.2\cos^2\alpha_{k1} d_{k1}}{GA_{dk1}} \tag{25}$$

$$\frac{1}{k_{ka}} = \int_{-\alpha_{k1}}^{\alpha_{k2}} \frac{\sin^2\alpha_{k1} r_{kb}\theta_k}{EA_{kx}} \mathrm{d}\alpha_k + \frac{\sin^2\alpha_{k1} d_{k1}}{EA_{dk1}} \tag{26}$$

The expressions of k_{kh} and k_{kf} remain unchanged as that in ***Situation A*** of ***Case 1***.

Case 2: The root circle is bigger than the base circle

Situation A: $\alpha_{k1} \ge \alpha_{kc}$

In this case, the potential energy stored in the part between root circle and base circle is not included in the calculation of the mesh stiffness. Figure 5 displays the spalled tooth model, whose root circle is bigger than base circle. The Hertzian stiffness maintains unchanged as that in ***Situation A*** of ***Case 1***, and the k_{kb}, k_{ks}, and k_{ka} have changed as:

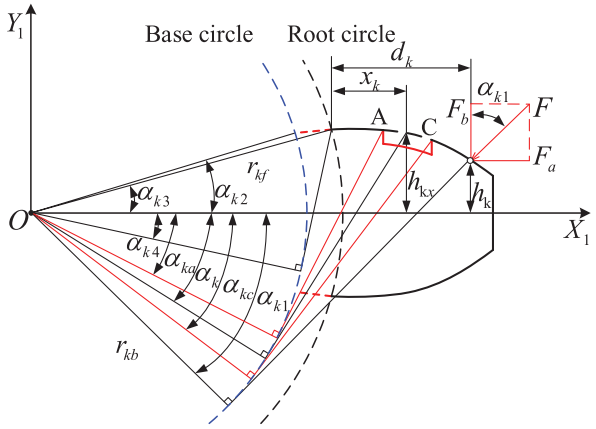

Fig. 5. Spalled sliced gear beam model when the root circle is bigger than base circle.

$$\frac{1}{k_{kb}}=\int_{-\alpha_{k1}}^{-\alpha_{kc}}\frac{[(d_k-x_k)\cos\alpha_{k1}-H_k]^2 r_{kb}\theta_k}{EI_{kx}}\mathrm{d}\alpha_k+\int_{-\alpha_{kc}}^{-\alpha_{ka}}\frac{[(d_k-x_k)\cos\alpha_{k1}-H_k]^2 r_{kb}\theta_k}{EI_{kxs}}\mathrm{d}\alpha_k+\int_{-\alpha_{ka}}^{-\alpha_{k4}}\frac{[(d_k-x_k)\cos\alpha_{k1}-H_k]^2 r_{kb}\theta_k}{EI_{kx}}\mathrm{d}\alpha_k \tag{27}$$

$$\frac{1}{k_{ks}}=\int_{-\alpha_{k1}}^{-\alpha_{kc}}\frac{1.2\cos^2\alpha_{k1} r_{kb}\theta_k}{GA_{kx}}\mathrm{d}\alpha_k+\int_{-\alpha_{kc}}^{-\alpha_{ka}}\frac{1.2\cos^2\alpha_{k1} r_{kb}\theta_k}{GA_{kxs}}\mathrm{d}\alpha_k+\int_{-\alpha_{ka}}^{-\alpha_{k4}}\frac{1.2\cos^2\alpha_{k1} r_{kb}\theta_k}{GA_{kx}}\mathrm{d}\alpha_k \tag{28}$$

$$\frac{1}{k_{ka}}=\int_{-\alpha_{k1}}^{-\alpha_{kc}}\frac{\sin^2\alpha_{k1} r_{kb}\theta_k}{EA_{kx}}\mathrm{d}\alpha_k+\int_{-\alpha_{kc}}^{-\alpha_{ka}}\frac{\sin^2\alpha_{k1} r_{kb}\theta_k}{EA_{kxs}}\mathrm{d}\alpha_k+\int_{-\alpha_{ka}}^{-\alpha_{k4}}\frac{\sin^2\alpha_{k1} r_{kb}\theta_k}{EA_{kx}}\mathrm{d}\alpha_k \tag{29}$$

Situation B: $\alpha_{ka}<\alpha_{k1}<\alpha_{kc}$
In this situation, the Hertzian stiffness is the same as that in ***Situation B*** of ***Case 1***. The expressions of k_{kb}, k_{ks}, and k_{ka} can be written as:

$$\frac{1}{k_{kb}}=\int_{-\alpha_{k1}}^{-\alpha_{ka}}\frac{[(d_k-x_k)\cos\alpha_{k1}-H_k]^2 r_{kb}\theta_k}{EI_{kxs}}\mathrm{d}\alpha_k+\int_{-\alpha_{ka}}^{-\alpha_{k4}}\frac{[(d_k-x_k)\cos\alpha_{k1}-H_k]^2 r_{kb}\theta_k}{EI_{kx}}\mathrm{d}\alpha_k \tag{30}$$

$$\frac{1}{k_{ks}}=\int_{-\alpha_{k1}}^{-\alpha_{ka}}\frac{1.2\cos^2\alpha_{k1} r_{kb}\theta_k}{GA_{kxs}}\mathrm{d}\alpha_k+\int_{-\alpha_{ka}}^{-\alpha_{k4}}\frac{1.2\cos^2\alpha_{k1} r_{kb}\theta_k}{GA_{kx}}\mathrm{d}\alpha_k \tag{31}$$

$$\frac{1}{k_{ka}}=\int_{-\alpha_{k1}}^{-\alpha_{ka}}\frac{\sin^2\alpha_{k1} r_{kb}\theta_k}{EA_{kxs}}\mathrm{d}\alpha_k+\int_{-\alpha_{ka}}^{-\alpha_{k4}}\frac{\sin^2\alpha_{k1} r_{kb}\theta_k}{EA_{kx}}\mathrm{d}\alpha_k \tag{32}$$

Situation C: $\alpha_{k1}\le\alpha_{ka}$
In this situation, the expressions of the mesh stiffness are the same as that in ***Situation A*** of ***Case 1***.

2) TVMS OF SPALLED GEARS. According to the derivation above, the k_h, k_b, k_s, k_a, and k_f of the spalled slice gear pair can be calculated. As for the healthy slice gear pair, the related derivation of mesh stiffness can be seen in [33]. Consequently, the mesh stiffness of the k^{th} slice gear pair is obtained as follows:

$$k_{kt}=\frac{1}{\frac{1}{k_{kh}}+\sum_{i=1}^{2}\left(\frac{1}{k_{kbi}}+\frac{1}{k_{kai}}+\frac{1}{k_{ksi}}+\lambda_i\frac{1}{k_{kfi}}\right)} \tag{33}$$

where subscript k represents the k^{th} slice gear. λ_i denotes the fillet foundation stiffness coefficient of the pinion ($i=1$) and the gear ($i=2$), which can be obtained with the method from [41].

The SBG is subjected to the action of space force during the meshing process. The axial force will cause axial deformation, whose influences on the mesh stiffness are usually nonnegligible. According to the decomposition of meshing force displayed in Fig. 6, the correction of meshing stiffness of the k^{th} slice tooth pair can be obtained from [42]:

$$k_{kn}=k_{kt}\cos^2\beta_k \tag{34}$$

Then, by summing the mesh stiffness of the slices participating in meshing process, the single-tooth mesh stiffness of SBG can be calculated, which can be expressed as follows:

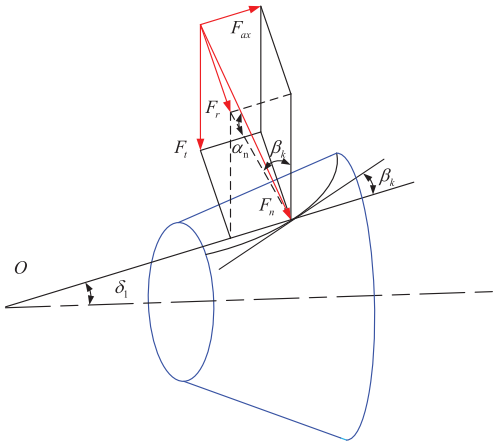

Fig. 6. Force decomposition of the SBG.

$$k = 1/\sum_{i=k_{\min}}^{k_{\max}} k_{kni} \tag{35}$$

where $k_{\min}$ is the minimum the number for the slices involved in the engagement process and $k_{\max}$ represents the maximum one.

For the SBGP with a contact ratio ranging from 2 to 3, double ($n = 2$) and triple ($n = 3$) pairs of gear teeth will take part in engagement in succession. Therefore, the TVMS of the SBG with spalling defect can be obtained as:

$$k_m = \frac{1}{\sum_j^n \frac{1}{k_j}} \tag{36}$$

where j represents the j^{th}pair of SBG tooth.

III. EFFECTS OF SPALLING DEFECT ON TVMS OF SBG

A. NUMERICAL SIMULATION AND RESULTS ANALYSIS

In this study, it is assumed that the spalling defect only occurs on one tooth of the pinion, and all other teeth on the pinion are perfect. Given the basic parameters of SBG as provided in Table I, the proposed method can be adopted to evaluate the single-tooth mesh stiffness and TVMS of the SBG under spalling defects. The size of spalling defect can be expressed by three variables: spalling length l_s, spalling width w_s, and depth h_s. Therefore, the spalls with different length, width, and depth are discussed. The sizes of different spalling severity levels are displayed in Table II. The effects of spalling defect on the mesh stiffness and TVMS are shown in Figs. 7–9.

Figures 7(a), 8(a), and 9(a) give the single-tooth mesh stiffness of different spalling sizes evaluated. And Figs. 7(b), 8(b), and 9(b) show the corresponding TVMS of SBG. It can be clearly observed that the existence of spalling defect reduces the amplitude of both single-tooth mesh stiffness and TVMS, and the more serious the spalling defect, the more the single-tooth mesh stiffness and TVMS is reduced. With the increase of spalling length, the maximum value of single-tooth mesh stiffness decreases by 3.77%, 7.09%, and 7.98% in three spalling severity levels, respectively. And the TVMS decreases by 3.82%, 7.47%, and 8.85% at the peak and by 9.30%, 14.95%, and 21.98% at the valley. For the three spalling width levels, the maximum value of single-tooth mesh stiffness decreases by 3.32%, 5.29%, and 7.98%, respectively. The TVMS decreases by 3.82%, 5.99%, and 8.85% at the peak, and by 13.24%, 18.38%, and 21.98% at the valley. For the three spalling depth levels, the reduction of maximum value of single-tooth mesh stiffness is 3.32%, 5.29%, and 7.98%, respectively. And the reduction of TVMS is 3.82%, 5.99%, and 8.85% at the peak, and 13.24%, 18.38%, and 21.98% at the valley.

However, when the spalling length is smaller than $0.75w$, the decline of the single-tooth mesh stiffness and TVMS is not prominent compared to the first two levels of spalling width and depth. It can be inferred that the influence of spalling length is larger than that of the spalling width and depth.

Table I. Main parameters of the SBG used in the simulation

Parameters	Pinion	Gear
Tooth number Z_1/Z_2	16	21
Modulus m_{et} (mm)	5	
Width of the tooth w (mm)	18	
Pressure angle α_n (°)	20	
Shaft angle $\sum$ (°)	90	
Mean spiral angle β_m (°)	35	
Pitch angle δ_1/δ_2 (°)	37.30	52.70
Addendum coefficient	0.85	
Young's modulus E (Pa)	2.07×10^{11}	
Shear modulus G (Pa)	7.96×10^{10}	
Discrete number of rotation angle N_s	1000	
Slice number N	100	
Cutter diameter D_0 (mm)	180	180

Table II. Spalling severity levels

Items	Spalling size
Length l_s $\left(h_s = 2\text{mm}, w_s = 2\text{mm}\right)$	0.5 w
	0.75 w
	w
Width w_s $(l_s = w, h_s = 2\text{mm})$	1 mm
	1.5 mm
	2 mm
Depth h_s $(l_s = w, w_s = 2\text{mm})$	1 mm
	1.5 mm
	2 mm

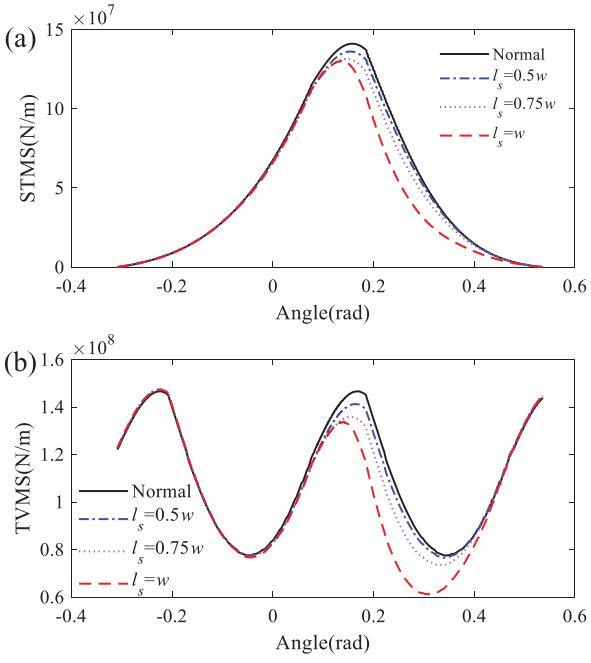

Fig. 7. Mesh stiffness of the SBG with different spalling length levels. (a) Single-tooth mesh stiffness (STMS) and (b) TVMS.

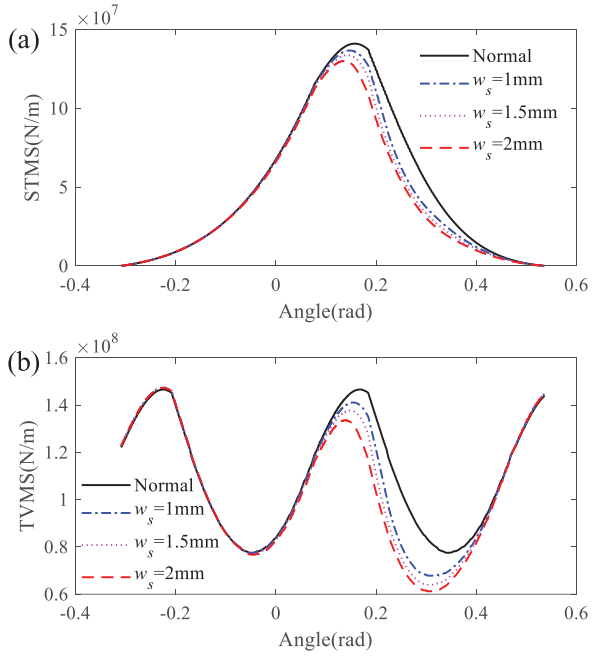

Fig. 8. Mesh stiffness of the SBG with different spalling width levels. (a) Single-tooth mesh stiffness (STMS) and (b) TVMS.

B. VERIFICATION BY FEM

To validate the proposed analytical model for the calculation of TVMS of SBG, a finite element model using SOLID185 elements is established as displayed in Fig. 10. The basic parameters of the SBG are given in Table I. The density of the gear material is 7850 kg/m^3, and the Poisson's ratio is 0.3.

The quasi-static algorithm [43] is used to complete the mesh stiffness simulation. In the finite element model, both

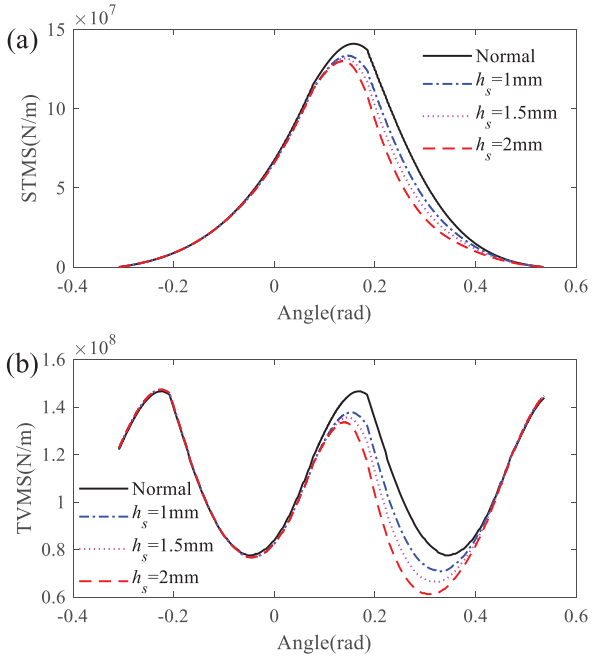

Fig. 9. Mesh stiffness of the SBG with different spalling depth levels. (a) Single-tooth mesh stiffness (STMS) and (b) TVMS.

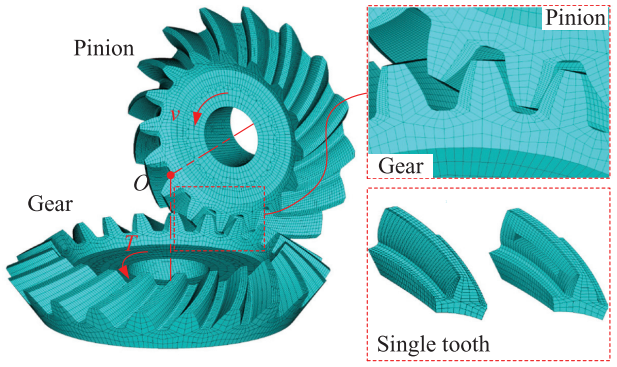

Fig. 10. 3D finite element model.

the pinion and gear have only one rotational DOF. The pinion is assigned a very low rotational speed, and a Z-axis torque T_g is applied to the driven gear. Finally, the rotation angular displacement of the pinion (φ_p) and gear (φ_g) can be solved, and the TVMS can be obtained as follows [37]:

$$k = \left| \frac{T_g}{R_g\left(R_p\varphi_p - R_g\varphi_g\right)} \right| \tag{37}$$

The TVMS acquired from the proposed method is compared with that obtained through FEM, which is depicted in Fig. 11. The spalling size of the model used in the comparison is spalling length $l_s = w$, spalling width $w_s = 2$mm, and spalling depth $h_s = 2$mm. It can be found that the TVMS curves calculated from the proposed method and FEM exhibit the same trend. The maximum error is 5.63% at the peak and 9.16% at the valley (obtained by $|k_{\text{theoretical\_calculation}} - k_{\text{FEM}}|/k_{\text{FEM}} \times 100\%$) when the gear set is perfect. For the gear set with spalling, the maximum error is 3.36% at the peak and 10.36% at the valley. The main reason which leads to the difference may be

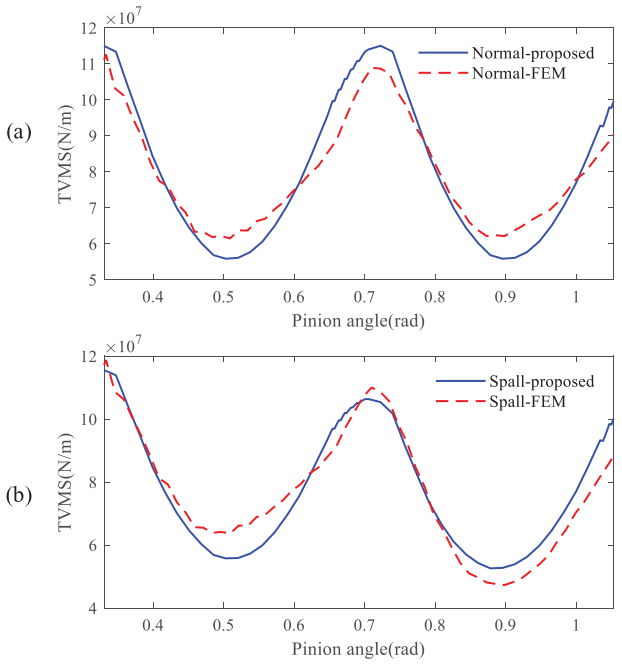

Fig. 11. TVMS comparison of the theoretical calculation and FEM. (a) Healthy state and (b) spalled state.

the three-dimensional solid model of the SBG pair and the finite element mesh generation quality of the teeth. Therefore, through the comparison with FEM, the proposed analytical model for the TVMS calculation of the SBG with spalling defect is verified.

VI. DYNAMIC MODELING OF SBG UNDER SPALLING DEFECT

A. LUMPED-PARAMETER MODEL

The lumped-parameter method has been widely used in dynamic modeling of gear system. According to the model proposed in [33], an 8-DOF dynamic model of SBG system is established with the use of the lumped-parameter method, which is displayed in Fig. 12. It is assumed that the two bodies of SBGP are rigid, and the shimmy of the gear is ignored. Besides, the direction of the meshing force F_m is the same as that of the normal force at the midpoint of tooth width. The coordinate system $S_o = (O,x,y,z)$ is established at the theoretical intersection of two bevel gear axes. The dynamic model comprises 8 DOF: $(x_1,y_1,z_1,\theta_1, x_2,y_2,z_2,\theta_2)^T$. x_1, y_1, and z_1 represent translational displacement of the pinion along the x, y, and z direction, the corresponding displacement of the gear is x_2, y_2, and z_2. θ_1 and θ_2 represent rotational displacement. m_1 and m_2 are the mass of the pinion and gear. T_{in} and T_{out} denote the input torque and the load moment acting on the pinion and gear, respectively. c_{xi}, c_{yi}, c_{zi} and k_{xi}, k_{yi}, k_{zi} $(i = 1,2)$ denote the equivalent support bearing damping and the equivalent support bearing stiffness in each direction of the pinion and gear, respectively. Along the line of action (LOA), the TVMS k_m, the meshing damping c_m, and the static transmission error $e(t)$ are coupled in the dynamic model.

The normal relative displacement along the LOA can be written as:

$$X_n = (x_1 - x_2)a_1 + (y_1 - y_2)a_2 + \left(z_1 - z_2 - r_{m1}\theta_1 + r_{m2}\theta_2\right)a_3 + e(t) \tag{38}$$

where the expressions of coefficients a_1, a_2, and a_3 can be obtained by follows:

$$\begin{cases} a_1 = \cos\delta_1 \cos\alpha_n \sin\beta_m \\ a_2 = \sin\delta_1 \cos\alpha_n \sin\beta_m - \cos\delta_1 \sin\alpha_n \\ a_3 = \cos\beta_m \cos\alpha_n \end{cases} \tag{39}$$

r_{m1} and r_{m2} represent the radius of pitch circle at the midpoint of tooth width of pinion and gear.

Therefore, the meshing force of the gear pair can be calculated as:

$$F_n = -k_m X_n - c_m \dot{X}_n \tag{40}$$

Decomposing the meshing force toward the coordinate axes, the component forces of the meshing force on each coordinate axis F_{xi}, F_{yi}, F_{zi} $(i = 1,2)$ can be obtained. The rotary inertia of the pinion and gear are I_1 and I_2, respectively. Thus, the differential equations of motion of the dynamic model could be written as follows:

$$\begin{cases} m_1\ddot{x}_1 + c_{x1}\dot{x}_1 + k_{x1}x_1 = F_{x1} \\ m_1\ddot{y}_1 + c_{y1}\dot{y}_1 + k_{y1}y_1 = F_{y1} \\ m_1\ddot{z}_1 + c_{z1}\dot{z}_1 + k_{z1}z_1 = F_{z1} \\ I_1\ddot{\theta}_1 + F_{z1}r_{m1} = T_{in} \\ m_2\ddot{x}_2 + c_{x2}\dot{x}_2 + k_{x2}x_2 = F_{x2} \\ m_2\ddot{y}_2 + c_{y2}\dot{y}_2 + k_{y2}y_2 = F_{y2} \\ m_2\ddot{z}_2 + c_{z2}\dot{z}_2 + k_{z2}z_2 = F_{z2} \\ I_2\ddot{\theta}_2 + F_{z2}r_{m2} = -T_{out} \end{cases} \tag{41}$$

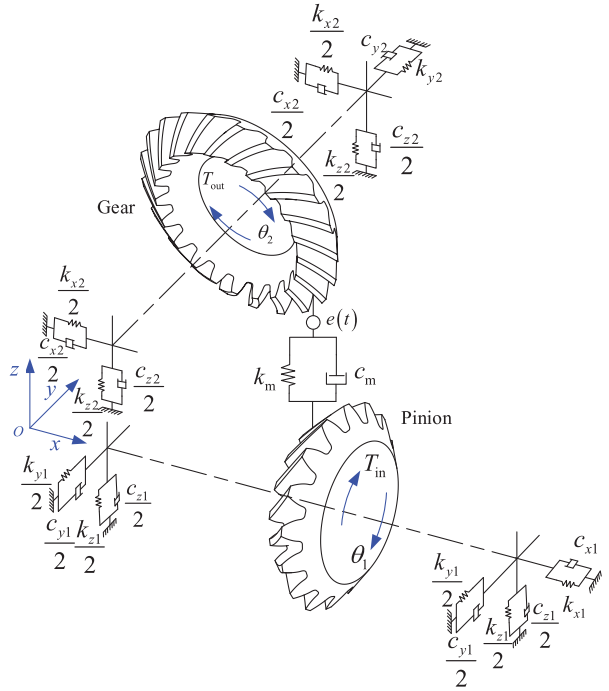

Fig. 12. Dynamic model of the SBG transmission system.

B. DYNAMIC RESPONSES

When the gear transmission suffers gear faults, its vibration responses contain the characteristic information of the faults [44,45]. To reveal the vibration characteristics of the SBG with spalling defect, the spalling fault is incorporated into the gear dynamic model through the TVMS deduced by slice method as a significant internal excitation. In order to conduct simulation of the SBG system with spalling defects, four various spalling degrees: no spalling, slight spalling ($l_s = 0.45w$, $w_s = 1$mm, $h_s = 1$mm) moderate spalling ($l_s = 0.5w$, $w_s = 1.25$mm, $h_s = 1.25$mm), and severe spalling ($l_s = 0.55w$, $w_s = 1.5$mm, $h_s = 1.5$mm) are considered in this study. With the simulation parameters provided in Table III, the Runge–Kutta method is employed to solve the dynamic model proposed in Fig. 12. The vibration responses can be acquired as shown in Figs. 13 and 14.

Table III. SBG system simulation parameters

Parameters	Values
Pinion rotation frequency f_r (Hz)	40
Meshing frequency f_m (Hz)	640
Input/output load T_{in}/T_{out} (Nm)	50/59
Sampling frequency f_s (kHz)	400

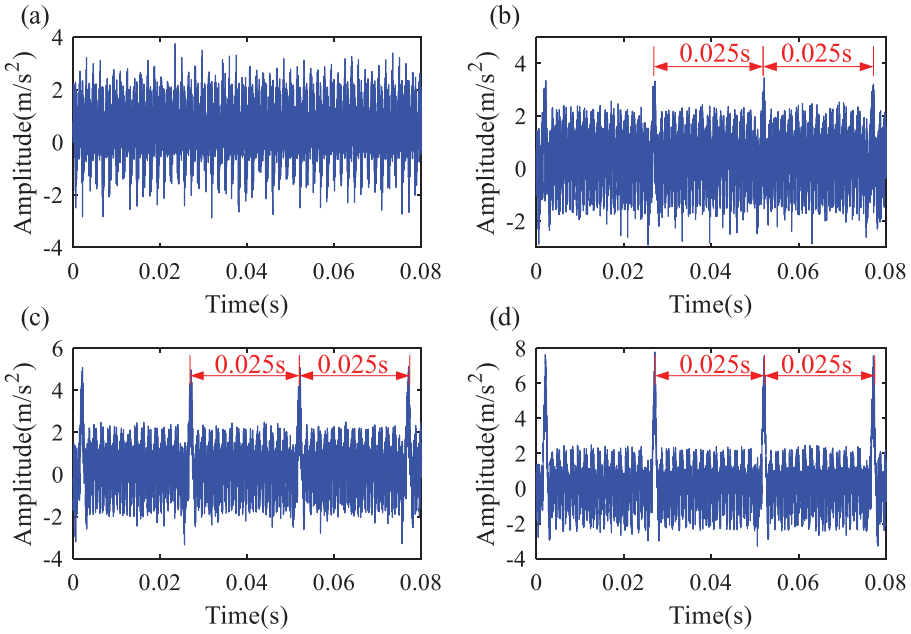

Fig. 13. Time-domain response with different spalling levels. (a) Normal, (b) slight damage, (c) moderate damage, and (d) severe damage.

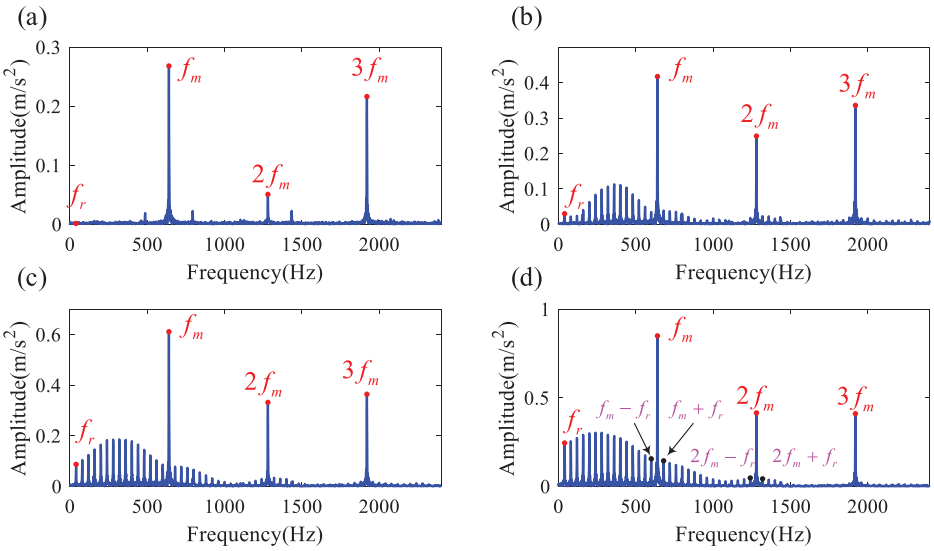

Fig. 14. Frequency-domain response with different spalling levels. (a) Normal, (b) slight damage, (c) moderate damage, and (d) severe damage.

Figure 13 illustrates the time-domain acceleration signals of the SBG under different spalling degrees. Figure 14 presents the corresponding amplitude spectra. It can be observed from the figures that for the perfect SBG, the time-domain signal is steady without any mutations, and only meshing frequency ($f_m = 640$Hz) and its harmonics appear in amplitude spectrum. While for the spalling state, the spalling fault causes periodic impulses in the time-domain responses, and the time interval between two adjacent impulses is 0.025 s, corresponding to the characteristic frequency of the spalled pinion (the pinion rotation frequency, $f_r = 40$Hz). The time-domain amplitude of the impulses becomes more obvious as the fault severity increases. Meanwhile, the frequency components of meshing frequency and its harmonics exhibit a significant increase in the amplitude spectra with the growth of the spalling severity. Besides, it can be observed that abundant sidebands with rotation frequency and its harmonics appear when the spalling begins to increase. Similarly, the sidebands become more abundant when the spalling fault gradually worsens. Figure 15 displays the zoomed frequency spectra in 0–300 Hz. The spectra line of 40 Hz bandwidth (equals to the rotation frequency of the spalled pinion) can be found, and the amplitude of the rotation frequency also increases obviously with the growth of the spalling fault severity.

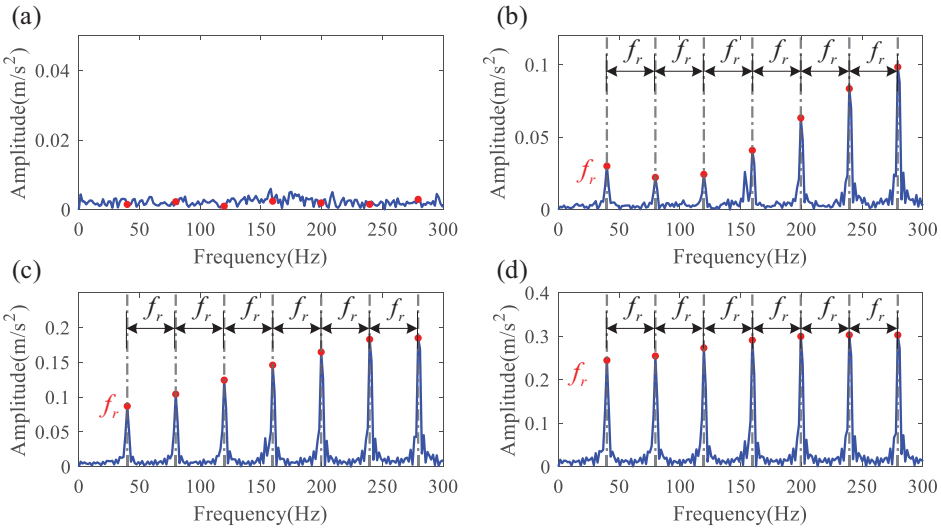

Fig. 15. Low-frequency spectra in 0 to 300 Hz. (a) Normal, (b) slight damage, (c) moderate damage, and (d) severe damage.

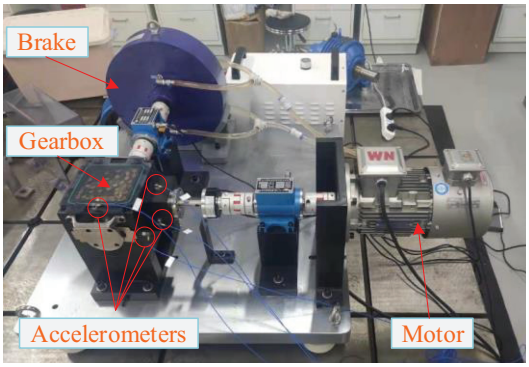

Fig. 16. Sensors on the gearbox of the test rig.

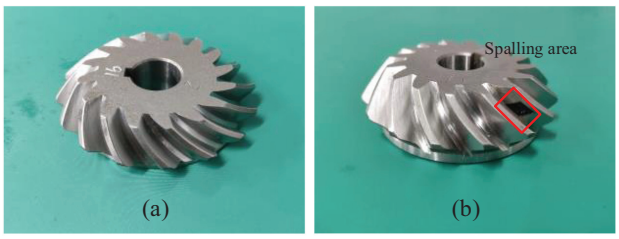

Fig. 17. Pinion used in the experiment. (a) Healthy condition and (b) spalled condition with size of: $l_s = 0.25w$, $h_s = 2$mm, $w_s = 4$mm.

C. EXPERIMENTAL VERIFICATION

The helicopter tail transmission test rig is used to validate the proposed model in this study. The test rig is composed of a drive motor, SBG, and brake, as shown in Fig. 16. Four accelerometers are placed nearby the bearing of transmission shaft, and then the acceleration can be collected. The teeth number of the gear pair in the gearbox is 16 and 21, which is consistent with the dynamic model. And the pinions in health and spalling states are used to conduct the experiments under the same working condition, which is depicted in Fig. 17. The sampling frequency of the experiments is set as 10240 Hz, and the pinion rotational frequency is 39.87 Hz. The experimental results of the health and spalling states are shown in Figs. 18 and 19.

In order to investigate the influences of spalling fault on frequency-domain results, the envelope spectrum is applied to analyze the simulation and experiment vibration signals. The results are presented in Fig. 20. It can be found that when spalling defect occurs, the amplitudes of fault frequency f_r and its harmonics have an obvious increase which are in line with those of the simulated signals shown in Fig. 15. The results of the simulation and experiment match well. There is a component at 30.38 Hz, which is the interference components caused by the rotation frequency of the driven gear.

Instantaneous energy is effective to enhance the time-domain impulse caused by spalling defect. In order to investigate the spalling impulse characteristics in time domain, instantaneous energy of the experimental vibration

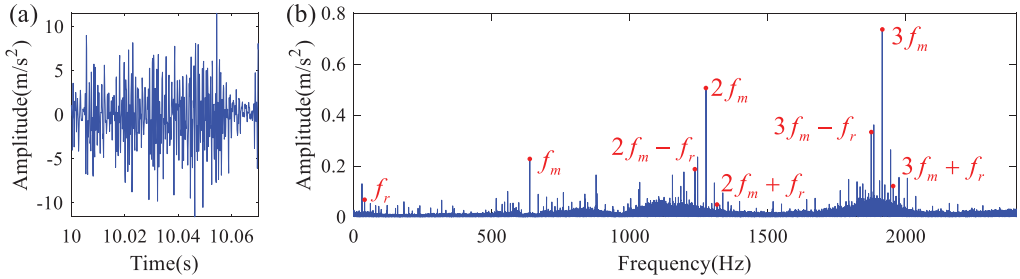

Fig. 18. Experiment results of the healthy condition. (a) Time-domain signal and (b) frequency spectrum.

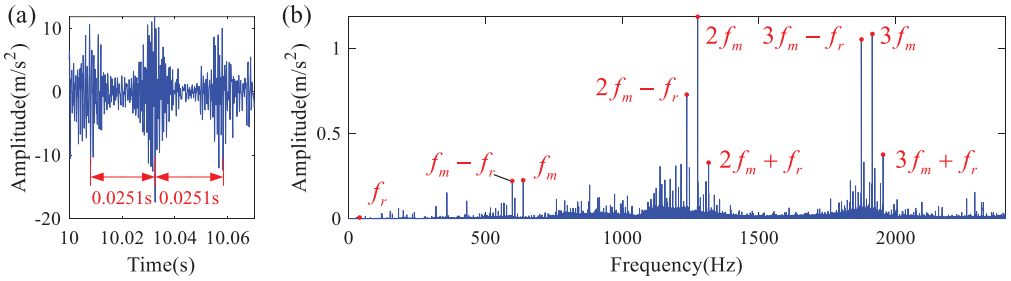

Fig. 19. Experiment results of the spalled condition. (a) Time-domain signal and (b) frequency spectrum.

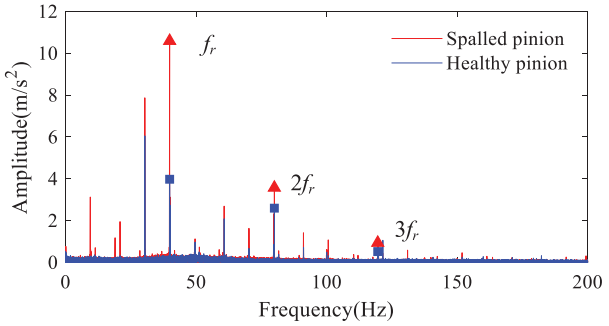

Fig. 20. Envelope spectrum comparison between the vibration signals in healthy and spalled conditions.

signals is calculated as given in Fig. 21. The calculation method of instantaneous energy can be seen in [46]. It can be observed from the figures that compared with the raw vibration signals, the instantaneous energy signals present evident impulses. The interval between two adjacent impulses is 0.251 s, which is corresponding to the spalled pinion rotation frequency 39.87 Hz. The experimental conclusion is in line with the simulation dynamic responses. Thus, the experimental results successfully verify the effectiveness and correctness of the proposed dynamic model of the SBG transmission system with spalling defect.

V. CONCLUSIONS

In this study, an analytical modeling method for the TVMS of the SBG with spalling defect is proposed based on the slice method. Then, the influences of spalling defect on the single-tooth stiffness and TVMS of SBG are revealed through a numerical simulation. An 8-DOF dynamical model of SBG transmission system is established with the consideration of TVMS and spalling defect. The simulated vibration responses are comprehensively analyzed in both time domain and frequency domain. Finally, the dynamic model is verified by the experiment results. The conclusions are drawn as follows.

With the introduction of the slice mothed, the potential energy method is employed to calculate the TVMS of healthy and spalled SBG. The effects of the spalling defect on single-tooth stiffness and TVMS are analyzed through numerical simulation. The results illustrate that the spalling length, width, and depth can cause reduction of the single-tooth stiffness and TVMS of SBG, and the single-tooth stiffness and TVMS can decrease more with the growth of spalling severity. Compared with the spalling width and depth, the influence of spalling length on the single-tooth and TVMS is smaller, especially when the spalling size is not significant. The FEM is used to validate the proposed method.

Incorporating the TVMS of spalling defect, an 8-DOF dynamic model of SBG system with spalling defect is established. And the dynamic responses are obtained and comprehensively analyzed in both time domain and frequency domain. The results show that the effect of the spalling defect in time domain is characterized by the impulse characteristic with an interval corresponding to the rotation frequency of the pinion with spalling defect. And the periodic impulse becomes more severe as the increasing spalling sizes. In addition, the spalling defect can cause the appearance of the sidebands in both sides of the meshing frequency and its harmonics. The sidebands become more intricate with the increase in the spalling defect.

The frequency spectrum, envelope spectrum, and instantaneous energy method are employed to obtain the

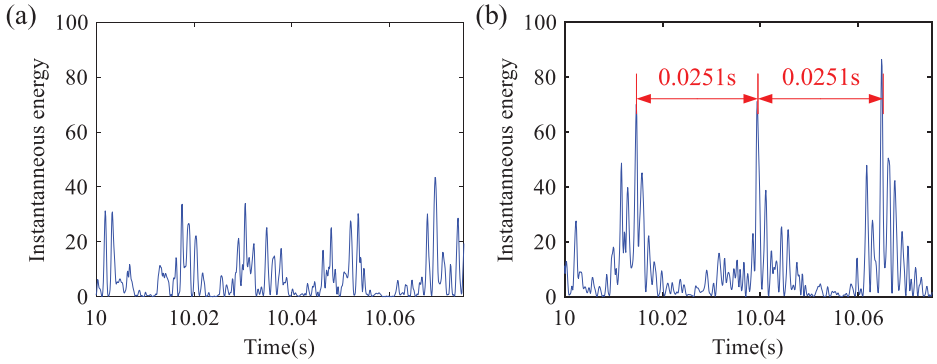

Fig. 21. Instantaneous energy signal. (a) Healthy condition and (b) spalled condition.

spalling defect characteristics from the experimental vibration signals. In the experimental results, the periodicity impulse with a period of 0.0251 s corresponding to the characteristics frequency (39.84 Hz) appears in time domain. The analysis results of experimental vibration signals are in line with the spalling defect characteristics calculated from the dynamic model, which indicates that the proposed analytical model is correct.

ACKNOWLEDGMENTS

This paper is supported by the National Natural Science Foundation of China (grant no. 52075414).

CONFLICT OF INTEREST STATEMENT

The authors declare no conflicts of interest.

REFERENCES

[1] H. Ding, S. Rong, K. Rong, and J. Tang, "Sensitive misalignment-based dynamic loaded meshing impact diagnosis mechanism for aviation spiral bevel gear transmission", *Expert. Syst. Appl.*, vol. 200, pp. 116969, 2022.

[2] Y. Mu, X. He, and Z. Fang, "An innovative ease-off flank modification method based on the dynamic performance for high-speed spiral bevel gear with high-contact-ratio", *Mech. Mach. Theory*, vol. 162, pp. 104345, 2021.

[3] J.-Y. Tang, Z.-H. Hu, L.-J. Wu, and S.-Y. Chen, "Effect of static transmission error on dynamic responses of spiral bevel gears", *J. Cent. South Univ.*, vol. 20, no. 3, pp. 640–647, 2013.

[4] T. Chen, Y. Wang, and Z. Chen, "A novel distribution model of multiple teeth pits for evaluating time-varying mesh stiffness of external spur gears", *Mech. Syst. Sig. Process.*, vol. 129, pp. 479–501, 2019.

[5] R. Huang, J. Xia, B. Zhang, Z. Chen, and W. Li, "Compound fault diagnosis for rotating machinery: state-of-the-art, challenges, and opportunities", *J. Dyn. Monit. Diagnost.*, vol. 2, no. 1, pp. 13–29, 2023.

[6] S. Wang, Y. Qin, D. Xi, and C. Liang, "U-shaped vision transformer and its application in gear pitting measurement", *J. Dyn. Monit. Diagnost*., vol. 4, no. 4, pp. 223–228, 2022.

[7] Y. Lei, Z. Liu, D. Wang, X. Yang, H. Liu, and J. Lin, "A probability distribution model of tooth pits for evaluating time-varying mesh stiffness of pitting gears", *Mech. Syst. Sig. Process*., vol. 106, pp. 355–366, 2018.

[8] J. Liu, C. Wang, and W. Wu, "Research on meshing stiffness and vibration response of pitting fault gears with different degrees", *Int. J. Rotating Mach.*, vol. 2020, pp. 1–7, 2020.

[9] X. Liang, H. Zhang, L. Liu, and M. J. Zuo, "The influence of tooth pitting on the mesh stiffness of a pair of external spur gears", *Mech. Mach. Theory*, vol. 106, pp. 1–15, 2016.

[10] X. Liang, M. J. Zuo, and Z. Feng, "Dynamic modeling of gearbox faults: a review", *Mech. Syst. Sig. Process.*, vol. 98, pp. 852–876, 2018.

[11] X. Kong, Z. Hu, J. Tang, S. Chen, and Z. Wang, "Effects of gear flexibility on the dynamic characteristics of spur and helical gear system", *Mech. Mach. Theory*, vol. 184, pp. 109691, 2022.

[12] Z. Sun, S. Chen, Z. Hu, and X. Tao, "Improved mesh stiffness calculation model of comprehensive modification gears considering actual manufacturing", *Mech. Mach. Theory*, vol. 167, pp. 104470, 2022.

[13] H. Li, S. Chen, J. Tang, Z. Sun, and Y. Hu, "Nonlinear dynamic modeling and analysis of spur gear based on gear compatibility conditions", *Mech. Mach. Theory*, vol. 167, pp. 1–17, 2022.

[14] F. Chaari, W. Baccar, M. S. Abbes, and M. Haddar, "Effect of spalling or tooth breakage on gearmesh stiffness and dynamic response of a one-stage spur gear transmission", *Euro. J. Mech.-A/Solids*, vol. 27, no. 4, pp. 691–705, 2008.

[15] R. Ma, Y. Chen, and Q. Cao, "Research on dynamics and fault mechanism of spur gear pair with spalling defect", *J. Sound Vib.*, vol. 331, no. 9, pp. 2097–2109, 2012.

[16] H. Jiang, Y. Shao, and C. K. Mechefske, "Dynamic characteristics of helical gears under sliding friction with spalling defect", *Eng. Fail. Anal.*, vol. 39, pp. 92–107, 2014.

[17] A. Saxena, A. Parey, and M. Chouksey, "Time varying mesh stiffness calculation of spur gear pair considering sliding friction and spalling defects", *Eng. Fail. Anal*., vol. 70, pp. 200–211, 2016.

[18] Y. Luo, N. Baddour, and M. Liang, "A shape-independent approach to modelling gear tooth spalls for time varying mesh stiffness evaluation of a spur gear pair", *Mech. Syst. Sig. Process.*, vol. 120, pp. 836–852, 2019.

[19] X. Wu, Y. Luo, Q. Li, and J. Shi, "A new analytical model for evaluating the time-varying mesh stiffness of helical gears in healthy and spalling cases", *Eng. Fail. Anal*., vol. 131, pp. 105842, 2022.

[20] K. Rong, B. Song, J. Wang, X. Qiu, G. Zhang, S. Rong, J. Tang, and H. Ding, "Higher-order parametrized correction based contact performance forecasting model for spiral bevel gears", *Mech. Syst. Sig. Process*., vol. 215, pp. 111434, 2024.

[21] H. Ding, X. Zou, S. Hua, Z. Zhou, G. Li, H. Liu, and J. Tang, "Carburizing effect-inspired bending fatigue forecasting model for spiral bevel gears", *Int. J. Mech. Sci.*, vol. 242, pp. 107987, 2023.

[22] H. Yang, W. Shi, Z. Chen, and N. Guo, "An improved analytical method for mesh stiffness calculation of helical gear pair considering time-varying backlash", *Mech. Syst. Sig. Process*., vol. 170, pp. 108882, 2022.

[23] Z. Chen and Y. Shao, "Dynamic simulation of spur gear with tooth root crack propagating along tooth width and crack depth", *Eng. Fail. Anal*., vol. 18, no. 8, pp. 2149–2164, 2011.

[24] Z. Wan, H. Cao, Y. Zi, W. He, and Y. Chen, "Mesh stiffness calculation using an accumulated integral potential energy method and dynamic analysis of helical gears", *Mech. Mach. Theory*, vol. 92, pp. 447–463, 2015.

[25] M. Feng, H. Ma, Z. Li, Q. Wang, and B. Wen, "An improved analytical method for calculating time-varying mesh stiffness of helical gears", *Meccanica*, vol. 53, no. 4–5, pp. 1131–1145, 2017.

[26] W. Yu and C. K. Mechefske, "A new model for the single mesh stiffness calculation of helical gears using the slicing principle", *Iran. J. Sci. Technol. Trans. Mech. Eng.*, vol. 43, no. S1, pp. 503–515, 2019.

[27] Q. Wang and Y. Zhang, "A model for analyzing stiffness and stress in a helical gear pair with tooth profile errors", *J. Vib. Control*, vol. 23, no. 2, pp. 272–289, 2016.

[28] R. Sun, C. Song, C. Zhu, X. Yang, and X. Li, "Computational study of pitting defect influence on mesh stiffness for straight beveloid gear", *Eng. Fail. Anal.*, vol. 119, pp. 104971, 2021.

[29] Z. Liu, F. Li, Z. Xu, and Q. He, "Semi-analytical loaded tooth contact analysis method for spiral bevel gears", *Int. J. Mech. Sci*., vol. 253, pp. 108329, 2023.

[30] S. Mo, Y. Li, D. Wang, X. Hu, H. Bao, G. Cen, and Y. Huang, "An analytical method for the meshing characteristics of asymmetric helical gears with tooth modifications", *Mech. Mach. Theory*, vol. 185, pp. 105321, 2023.

[31] S. D. Yavuz, Z. B. Saribay, and E. Cigeroglu, "Nonlinear time-varying dynamic analysis of a spiral bevel geared system", *Nonlinear Dyn.*, vol. 92, no.4, pp. 1901–1919, 2018.

[32] J. J. Yang, Z. H. Shi, H. Zhang, T. X. Li, S. W. Nie, and B. Y. Wei, "Dynamic analysis of spiral bevel and hypoid gears with high-order transmission errors", *J. Sound Vib.*, vol. 417, pp. 149–164, 2018.

[33] L. Yinong, L. Guiyan, and Z. Ling, "Influence of asymmetric mesh stiffness on dynamics of spiral bevel gear transmission system", *Math. Probl. Eng.*, vol. 2010, pp. 1–13, 2010.

[34] W. Cao, W. Pu, and J. Wang, "Tribo-dynamic model and fatigue life analysis of spiral bevel gears", *Euro. J. Mech.-A/Solids*, vol. 74, pp. 124–138, 2019.

[35] S. Chen, A. Zhang, J. Wei, and T. C. Lim, "Nonlinear excitation and mesh characteristics model for spiral bevel gears", *Int. J. Mech. Sci.*, vol. 257, pp. 108541, 2023.

[36] M. Molaie, F. S. Samani, A. Zippo, and F. Pellicano, "Spiral bevel gears: nonlinear dynamic model based on accurate static stiffness evaluation", *J. Sound Vib.*, vol. 544, pp. 117395, 2023.

[37] Y. Wang, H. Wang, K. Li, B. Qiao, Z. Shen, and X. Chen, "An analytical method to calculate the time-varying mesh stiffness of spiral bevel gears with cracks", *Mech. Mach. Theory*, vol. 188, pp. 105399, 2023.

[38] X. Liang, M. J. Zuo, and M. Pandey, "Analytically evaluating the influence of crack on the mesh stiffness of a planetary gear set", *Mech. Mach. Theory*, vol. 76, pp. 20–38, 2014.

[39] W. Luo, B. Qiao, Z. Shen, Z. Yang, H. Cao, and X. Chen, "Investigation on the influence of spalling defects on the dynamic performance of planetary gear sets with sliding friction", *Tribol. Int.*, vol. 154, pp. 106639, 2021.

[40] P. Sainsot, P. Velex, and O. Duverger, "Contribution of gear body to tooth deflections—a new bidimensional analytical formula", *J. Mech. Des.*, vol. 126, no. 4, pp. 748–752, 2004.

[41] H. Ma, J. Zeng, R. Feng, X. Pang, and B. Wen, "An improved analytical method for mesh stiffness calculation of spur gears with tip relief", *Mech. Mach. Theory*, vol. 98, pp. 64–80, 2016.

[42] J. Wei, A. Zhang, G. Wang, D. Qin, T. C. Lim, Y. Wang, and T. Lin, "A study of nonlinear excitation modeling of helical gears with modification: theoretical analysis and experiments", *Mech. Mach. Theory*, vol. 128, pp. 314–335, 2018.

[43] J. Zhang, M. Fard, and R. Jazar, "A CAD-FEM-QSA integration technique for determining the time-varying meshing stiffness of gear pairs", *Measurement*, vol. 100, pp. 139–149, 2017.

[44] D. Zhang and Z. Feng, "Wind turbine planetary gearbox fault diagnosis via proportion-extracting synchrosqueezing chirplet transform", *J. Dyn. Monit. Diagnost.*, vol. 2, no. 3, pp. 177–182, 2023.

[45] Y. Han, X. Chen, J. Xiao, J. X. Gu, and M. Xu, "An improved coupled dynamic modeling for exploring gearbox vibrations considering local defects", *J. Dyn. Monit. Diagnost.*, vol. 2, no. 4, pp. 262–274, 2023.

[46] F. S. Samani, M. Molaie, and F. Pellicano, "Nonlinear vibration of the spiral bevel gear with a novel tooth surface modification method", *Meccanica*, vol. 54, no. 7, pp. 1071–1081, 2019.